Impact of Platinum Loading and Catalyst Layer Structure on PEMFC Performance

Jon P. Owejan,[a,b,c,z] Jeanette E. Owejan,[a] and Wenbin Gu[a,*]

[a]*General Motors Electrochemical Energy Research Laboratory, Honeoye Falls, New York 14472, USA*
[b]*University of Tennessee at Knoxville, Department of Mechanical Engineering, Knoxville, Tennessee 37916, USA*

Reducing Pt in proton exchange membrane fuel cells is the subject of intense research and development. Recently, researchers have observed significant performance loss due to a transport limitation at the Pt surface. This is investigated here with loading studies that fix electrode thickness and bulk properties. Within these layers, the impact of Pt dispersion is probed by varying the wt% of Pt/C while holding Pt loading and electrode thickness constant by diluting with carbon, effectively varying the average distance between Pt particles while maintaining gas phase loss in the catalyst layer. Results elucidate how the electrode structure impacts local transport loss. It is demonstrated that local transport loss is not fully captured with a normalized Pt area. Additional geometric considerations that account for ionomer surface area relative to the Pt particles are required to resolve performance loss at low Pt loading as electrode structure varies. Furthermore, within this ionomer layer an interfacial resistance at both the gas and Pt interfaces are necessary to account for performance trends observed. These results demonstrate that residual performance loss associated with low cathode Pt loading can be mitigated by electrode design, where oxygen flux through the gas/ionomer interface to the Pt surface is minimized.

In the current paradigm of low cost internal combustion engine powered personal transport, fuel cell stacks with Pt loadings equivalent to greater than 0.15 g_{Pt} kW^{-1} will not be cost competitive. As a result, fuel cell researchers are exploring the limits of Pt loading with established catalyst structures[1–5] in parallel with advanced catalyst research.[6–8] This work has identified several challenges that arise in practical PEMFC systems when Pt is used sparingly. First, when the electrode structure is made thinner to reduce Pt loading, water management, particularly during transients, can limit performance.[9,10] Second, as local current density at the Pt surface increases with decreased loading, resulting in a lower cell voltage, the oxygen reduction reaction (ORR) rate stops following simple Tafel kinetics and becomes potential-dependent.[11] Third, for ionomer coated catalysts, an additional transport resistance from the electrode pore to the Pt surface has been reported that is much higher than oxygen permeability through bulk ionomer.[12–14]

This article details an investigation of the third challenge - using a series of experiments that attempt to isolate key components of the catalyst layer design that impact local transport performance. Maintaining a constant catalyst layer thickness and macroscopic structure, the impact of loading and Pt dispersion was studied with performance and limiting current methods. These results are then used to consider key parameters that impact the performance loss at low Pt loading. Further insight is obtained by scaling the variations in the total transport resistance measured with limiting current to Pt surface area. For a constant pore structure, this analysis isolates oxygen transport loss at the Pt surface independently of bulk and Knudsen diffusion effects.[15]

There is significant discussion in recent literature about the parameters being studied herein. The most obvious is the oxygen permeability in thin Nafion films vs. bulk; however due to the difficult nature of this measurement there are no reported data currently available at the length scales of interest (less than 30 nm). While direct measurements of oxygen transport resistance are elusive, researchers have recently focused on related parameters. Although the change in physical properties of these films is established,[16–20] the water/polymer morphology and related stiffness are not. Several research groups have reported interfacial interactions of thin Nafion films that are unique to the supporting substrate.[21,22] These experiments generally report lower uptake in thin films than bulk but there is significant variation in the magnitude of the decrease reported. In more applied experiments,

Iden et al. reported similar uptake relative to bulk in actual catalyst layers.[23] Perhaps analogous to water uptake, there is also significant variation in proton conductivity reported for thin Nafion films.[24–26]

Understanding local transport resistance also requires consideration of the complex structure of dispersed Pt on carbon and ionomer system. The one-dimensional relationships described previously capture key parameters for an idealized system but the catalyst layer does not have a homogeneous pore structure. In fact, significant heterogeneities exist in the catalyst layer due to mesoscale defects in the primary carbon particle and aggregation.[27,28] These agglomerates introduce new transport domains relative to the assembled macroporous catalyst layer. Unfortunately it is difficult to decouple the impact of the mesoscale structure inside the agglomerate relative to the outer surface that has more direct access to the oxidant within the macro pores of the catalyst layer. This agglomerate relationship is widely studied with transport modeling;[28–34] however, without direct validation, the physical theory and input parameters vary significantly in these proposed models. The experiments described in this article aim to consider the relative influences of parameters related to local transport at the Pt nano particle, where samples are designed such that mesoscale and agglomeration effects are consistent across all configurations. To interpret the experimental results, limiting current at an individual Pt particle based on oxygen transport through the ionomer is modeled to consider the role of interfacial resistances.

Experimental

Cathode catalyst layer loading and density of platinized aggregates were varied while maintaining thickness by mixing various weight percentages of Pt on Vulcan XC-72 catalysts and adding additional bare Vulcan XC-72 when necessary. The resulting structure, illustrated in Figure 1, will impact oxygen flux near the Pt sites while maintaining a similar macroporous catalyst layer structure. This study represents a significant experimental campaign that includes 12 cathode electrode configurations, with 3 samples of each run in 3 separate fuel cells with a consistent experimental protocol throughout. Three different test stands and hardware sets were used for each electrode type to enable a statistical data summary that included test stand and hardware variation. Table I lists the experimental protocol used in each experiment. The catalyst layer thickness was kept constant (within capability of the coating method) throughout this experimental campaign to reduce bulk transport differences between the samples.

Electrochemical characterization.— Hydrogen adsorption/desorption (HAD) area was measured with cyclic voltammetry

*Electrochemical Society Active Member.
[c]Present address: SUNY-Alfred, Department of Mechanical Engineering Technology, Alfred, New York 14802, USA.
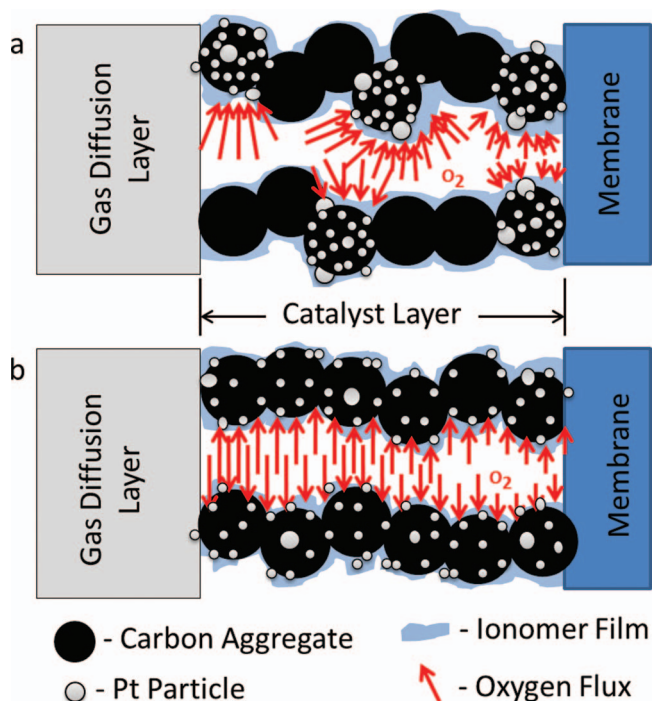[z]E-mail: owejanjp@alfredstate.edu

Figure 1. Catalyst layer structure resulting from a.) 50% wt Pt/Vulcan diluted with bare Vulcan, and b.) mixing varied wt% Pt/Vulcan catalysts. Not to scale, HAD area indicates Pt particles vary as much as 1.5x in low vs. high wt% Pt/Vulcan catalysts.

on limiting current at different total pressures with varied oxygen concentrations.[15] Lastly, impedance was used to measure membrane and electrode proton transfer resistances as described by Liu et al.[37] Also shown in Table I, a voltage recovery step was run periodically throughout the protocol. This step serves to remove contaminates and Pt-oxides from the catalyst surface. For low Pt loading performance studies, a consistent voltage recovery scheme will improve consistency between experiments.[38]

Materials.— Table II details key experimental parameters that were constant in all experiments. All 5 cm^2 membrane electrode assemblies (MEAs) were fabricated using the decal transfer process, detailed previously.[36] However, all ionomer was kept in the acid form throughout fabrication procedure. Cathode electrodes at the following loadings were fabricated: 0.3, 0.2, 0.1, 0.05, and 0.025 mg$_{Pt}$ cm^{-2}. Starting at 0.1 mg$_{Pt}$ cm^{-2} and for all lower loadings, at least 2 types of cathode electrodes were made. The first was made from a 50 wt% Pt/Vulcan catalyst and diluted with Vulcan XC-72 carbon while the others consisted of one or more lower wt% catalysts such that each carbon particle was platinized and a constant catalyst layer thickness could be maintained. All these electrodes were fabricated using either one or more of the following components: 5, 10, 15, 20, 30, and 50 wt% Pt/Vulcan (TKK) and Vulcan carbon support, along with DuPont D2020 ionomer at an ionomer to carbon weight ratio of 0.95. To further study the lowest loading, additional 0.025 mg$_{Pt}$/cm^2 electrodes were made by varying the amount of platinized carbon particles. Thickness was again maintained by adding the Vulcan carbon black to different wt% Pt/Vulcan catalysts.

A summary of all cathode catalyst layer formulations used in this study is provided in Table III. Scanning electron microscope (SEM) images were taken of cross-sections from each decal in 3 locations (5 images per location, for a total of 15 thickness measurements per type) to estimate the catalyst layer thickness and uniformity, also given in Table III. Since the carbon type, I/C ratio, and coating method were consistent for all samples, the porosity was expected to have negligible variation. Thickness variation was minimized for a given loading, and slight variation in solids content was accounted for by weighing the decal before and after lamination. These actual loadings were used to normalize the measured Pt surface area. SEM images were also taken in field emission mode to contrast platinized from bare carbon and open structure. Example images from this SEM cross sectional analysis are given in Figure 2. The average cross-sectional area of platinized carbon aggregates was estimated from the field emission SEM images (Figure 2b) by counting the number of adjacent high contrast pixels (due to Pt content) and scaling based on pixel size (Figure 2c). This analysis demonstrated that the platinized carbon aggregates have a similar average cross-sectional area and their distribution is uniform through the thickness of the catalyst layer for the various catalyst configurations used. This indicates that the electrodes diluted

before and after the performance protocol was run on each cell build. Cathode Pt-surface area was measured by integrating hydrogen adsorption peaks (assuming 210 μC cm^{-2}$_{Pt}$). The conditions of CV measurement were 30°C; 100% H$_2$ in anode and with the cathode channels filled with liquid water. The liquid water that fills the cathode helps maintain hydrogen partial pressure by preventing any hydrogen (crossing over from anode) from diffusing away from the cathode. This prevents the H$^+$ adsorption peaks (required for Pt surface area analysis) from being masked by the hydrogen evolution current.[35] Shorting resistance and hydrogen evolution current resulting from hydrogen cross-over was also measured in separate experiments with H$_2$/N$_2$.

After this initial characterization, several polarization curves were gathered in both oxygen and air to characterize mass activity[36] and consider the relative impact of water activity and temperature in the electrode. The total transport resistance is later derived based

Table I. Experimental protocol used in all experiments with constant differential flow conditions using 15/20 H$_2$/air stoichiometric ratios.

Experimental	Details
SEM Cross Section	Freeze fractured cross section in 3 locations of each cathode formulation
HAD	20°C; H$_2$ / liquid water; 200 mV/s; 0-600 mV
Break-in	Wet and dry cycling between low and high current density
Cathode Recovery	2 Hours at 0.300 V; 40°C; 100% RH; 150 kPa
O$_2$ Pol Curve	100% O$_2$; 100% RH; 80°C; 150 kPa
Air Pol Curve	21% O$_2$ 79% N$_2$; 100% RH; 80°C; 150 kPa
Cathode Recovery	2 Hours at 0.300 V; 40°C; 100% RH; 150 kPa
Air Pol Curve	80°C; 65%RH; 150 kPa
Air Pol Curve	93.5°C; 65%RH; 250 kPa
Cathode Recovery	2 Hours at 0.300 V; 40°C; 100% RH; 150 kPa
Limiting Current	Varied P$_{O2}$; 80°C; 80% RH; 110 kPa
Limiting Current	Varied P$_{O2}$; 80°C; 71% RH; 150 kPa
Limiting Current	Varied P$_{O2}$; 80°C; 67% RH; 200 kPa
Limiting Current	Varied P$_{O2}$; 80°C; 64% RH; 300 kPa
Impedance	H$_2$/N$_2$; 35; 50; 75; 122% RH; 0.2 V; const P$_{H2}$ and P$_{N2}$ = 253 kPa

Table II. Constant parameters in all experiments.

Parameter	Details
Anode Catalyst Layer	0.05 mg Pt/cm^2, 0.6 ionomer to carbon weight ratio electrode, comprised from a 20 wt% Pt/Vulcan XC-72 catalyst from Tanaka Kikinzoku Kogyo (TKK), Japan, and Nafion D2020 ionomer from DuPont (DuPont, USA)
Membrane	W.L. Gore 18 μm
MEA Lamination	146°C, 4 min, 18 kN
Gas Diffusion Layer	Mitsubishi Rayon Co. U-105 (5 wt% PTFE) with MPL
Gas Flow Distributor	Straight pass, 0.5 mm channel width, 0.5 mm land width, 0.7 mm depth {method ref. 2}
Active Area	5 cm^2
Cathode Catalyst Layer Ionomer to Carbon	0.95 by weight
Compression	20% strain controlled with fixed displacement

with bare carbon are well mixed and there was no obvious segregation of the platinized carbon (beyond the aggregate size). With this established for constant thickness catalyst layers, the influence of wt% of Pt on Vulcan was probed with the assumption that gas phase transport resistance through the catalyst layer is constant in all samples.

Results

Results to follow are represented by the mean of the 3 experimental runs executed for each catalyst layer type and all reported error is based on 95% confidence intervals for this mean. The key electrochemical characterization results for all samples examined in this study are provided in Figure 3. Ideally, the measurements in Figure 3a-3e would be constant as this will avoid convolving the focus of this study, transport loss near the Pt surface. Of these measurements, the variation in Pt area measured from HAD cyclic voltammetry is most significant. This variation of nearly 30% results from differences in the mean Pt particle size which was measured with X-ray diffraction (XRD) for the catalysts used in this study. HAD areas calculated based on the mean Pt diameter from XRD (4.9 nm) verify the measurement within 5%, and the trend in Pt area is independently verified in Figure 3b where the mass activity follows a similar but less pronounced trend. In addition of characterizing the platinized carbon aggregate distribution in the cross-section of diluted electrodes with SEM, the Pt particle size distributions for each catalyst type were also characterized with scanning transmission electron microscopy (STEM). STEM results indicate that lower HAD areas are influenced by infrequent localized large Pt aggregates that have a significant impact on the mean. At 2.0 A cm^{-2}, using a Tafel slope of 140 mV decade^{-1},[11] this variation in Pt area/activity would account for less than ±10 mV performance

difference between all samples at a given loading, assuming no local resistance.

For the MEAs used in this work, high frequency resistance (HFR) was obtained at 8 kHz, and cathode catalyst layer (11 ± 1.5 μm thick cathode regardless of Pt loading and/or dilution, see Table III) proton transfer resistances were relatively constant at 0.048 ± 0.003 and 0.014 ± 0.004 ohm cm^2 respectively at the conditions used for fully humidified polarization measurements at 80°C. At these conditions, the losses from electrode proton transfer are less than 14 ± 4 mV [39] at the highest current densities (2.0 A cm^{-2}); thus non-polarizing membrane and contact resistances (HFR) dominate the ohmic corrections applied to the cell potential. Since electrode proton resistance is relatively consistent between samples at 122% RH (Figure 3d), a drier condition at 50% RH is given in Figure 3c to highlight the relative differences between samples and estimate the performance impact (±10 mV) at the dry operating condition discussed later in this article.

The oxygen diffusion resistance in the bulk of the porous diffusion media is represented by the ratio of oxygen diffusion coefficients without and with porosity and tortuosity effects (D/D$_{eff}$) in Figure 3e, which is calculated from limiting current at different total pressures.[15] Since the same GDL and macroporous catalyst layer structure was used in all experiments, this parameter should not vary significantly between configurations. This is the case in Figure 3e as all data lie within uncertainty, thus verifying that bulk diffusion is relatively constant. When corrected for, this variation in diffusion resistance has a maximum voltage correction variance of ±5 mV.[40] Summing these variations for bulk diffusion, electrode proton resistance, and Pt surface area results in an error of ±20 mV at 2.0 A cm^{-2} at fully humidified conditions and up to ±27 mV at 50% RH. This maximum

Table III. Catalyst layer formulation variables and SEM characterization.

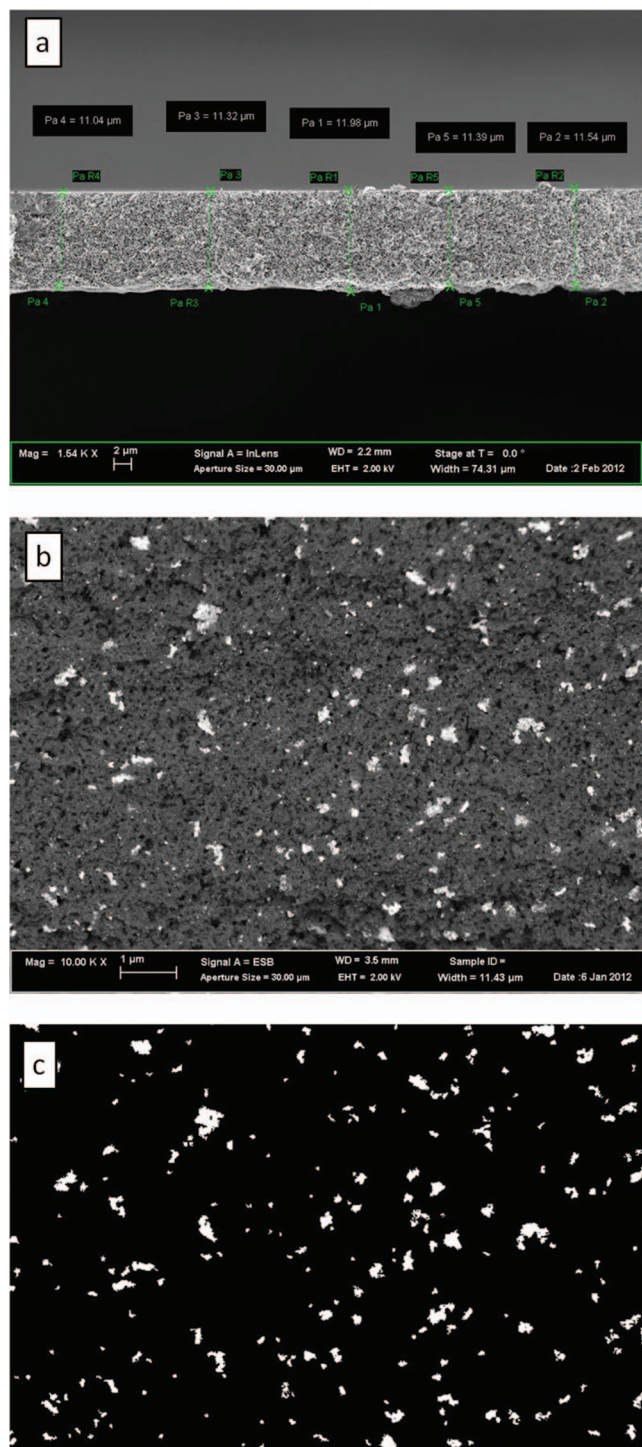|			Catalyst Layer Formulation			SEM Characterization	
Sample	Pt Loading (mg cm^{-2})	Carbon Dilution	Catalyst Type; fraction of catalyst type in overall catalyst wt Fraction	Catalyst Type; fraction of catalyst type in overall catalyst wt Fraction	Bare Carbon Fraction	Thickness (μm)	Average Platinized Aggregate Cross Sectional Area (μm^2)
1	0.3	No	50% Pt/V; 0.80	10% Pt/V; 0.20	-	9.7 ± 0.2	0.016
2	0.2	No	50% Pt/V; 0.56	20% Pt/V; 0.44	-	9.2 ± 0.8	0.014
3	0.1	No	15% Pt/V; 0.71	30% Pt/V; 0.29	-	10.4 ± 1.8	0.012
4	0.1	Yes	50% Pt/V; 0.42	-	0.58	10.9 ± 0.6	0.016
5	0.05	No	10% Pt/V; 1.0	-	-	11.2 ± 1.1	0.012
6	0.05	Yes	50% Pt/V; 0.22	-	0.78	13.1 ± 0.8	0.016
7	0.025	No	5% Pt/V; 1.0	-	-	11.0 ± 1.2	0.015
8	0.025	Yes	5% Pt/V; 0.34	10% Pt/V; 0.34	0.33	10.8 ± 0.3	0.015
9	0.025	Yes	10% Pt/V; 0.51	-	0.49	10.7 ± 0.5	0.012
10	0.025	Yes	15% Pt/V; 0.34	-	0.66	10.4 ± 0.4	0.011
11	0.025	Yes	30% Pt/V; 0.18	-	0.82	11.3 ± 0.5	0.013
12	0.025	Yes	50% Pt/V; 0.11	-	0.89	12.2 ± 0.8	0.016

Figure 2. Freeze fracture SEM cross-sectional analysis of a.) thickness, b.) field emission mode contrasting Pt to C, c.) platinized aggregate size and distribution analysis. Shown for the 0.025 mg$_{Pt}$ cm^{-2} catalyst layer.

Figure 3. Summary of key measurements characterizing all electrode types a.) Pt surface area measured with hydrogen/liquid water cyclic voltammetry,[33] b.) Pt mass activity measured at 0.9 V in pure oxygen at 80°C and 100% RH,[34] c.) electrode proton resistance measured with impedance (50% RH condition shown),[35] d.) electrode proton resistance measured with impedance (122% RH condition shown),[35] e.) effective oxygen diffusion coefficient measured based on pressure dependence of limiting current at <100% RH conditions,[15] f.) Pt area normalized to the geometric active area (loading * HAD area), g.) pressure independent transport resistance from limiting current at <100% RH conditions. Error bars represent 95% confidence intervals for the mean.

occur at or near the Pt surface, this component of resistance ($R_{O_2}^{Pt/i}$) is assumed to scale inversely with the normalized Pt area per Equation 1. This assumption is good when the local resistance is high enough to result in relatively uniform reaction current distribution.[41] Based on Equation 1, $R_{O_2}^{Knudsen}$ is determined from the intercept of the $R_{O_2}^{P,ind.}$ vs. $A_{active\ area}/A_{Pt,\ surf}$ relationship that is generated experimentally by varying Pt loading. The total transport resistance ($R_{O_2}^{total}$) also includes the pressure dependent bulk diffusion resistance (characterized in Figure 3e) that is given in Equation 2.

$$R_{O_2}^{P,ind} = R_{O_2}^{Knudsen} + \frac{A_{active\ area}}{A_{Pt,surf}} R_{O_2}^{Pt/i} \qquad [1]$$

$$R_{O_2}^{total} = R_{O_2}^{P,dep} + R_{O_2}^{P,ind} \qquad [2]$$

The total transport resistance at limiting current (I_{lim}) is given by Equation 3 when the oxygen concentration at the Pt surface ($C_{O_2,Pt}$) is near zero.

$$\frac{I_{\lim}}{4F} = \frac{C_{O_2,channel} - C_{O_2,Pt}}{R_{O_2}^{total}} \approx \frac{C_{O_2,channel}}{R_{O_2}^{total}} \qquad [3]$$

error between samples is considered when comparing uncorrected performance data.

The functionality of pressure independent transport resistance given in Figure 3g with the normalized Pt area (*loading × HAD area* $= A_{Pt,\ surf}/A_{active\ area}$) given in Figure 3f is the focus of the current study. Based on the limiting current analysis, the pressure independent oxygen transport resistance ($R_{O_2}^{P,ind.}$) is assumed to consist of Knudsen ($R_{O_2}^{Knudsen}$) and interfacial effects. Since an interfacial resistance would
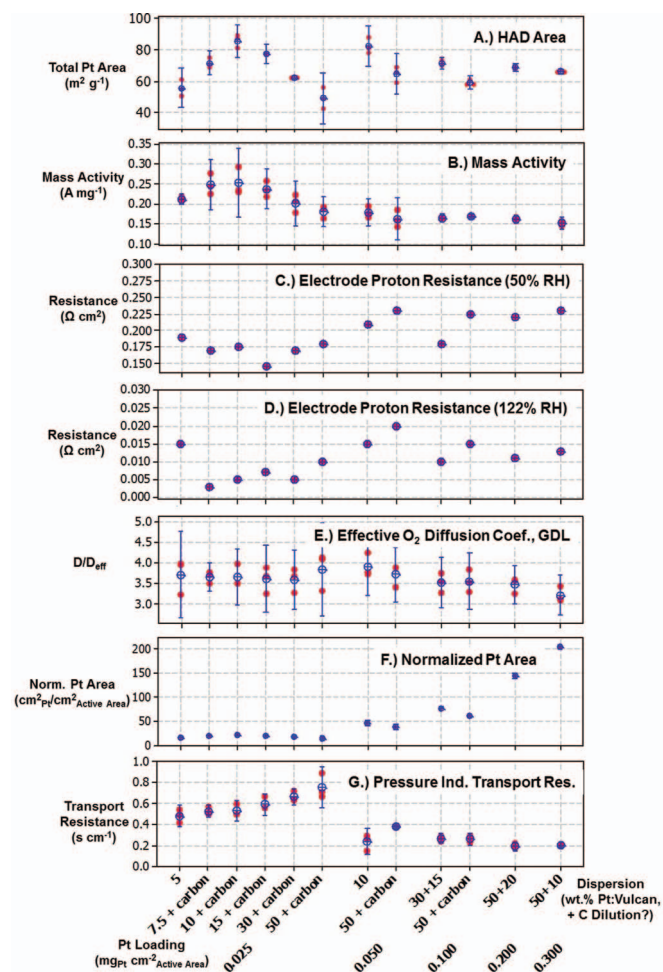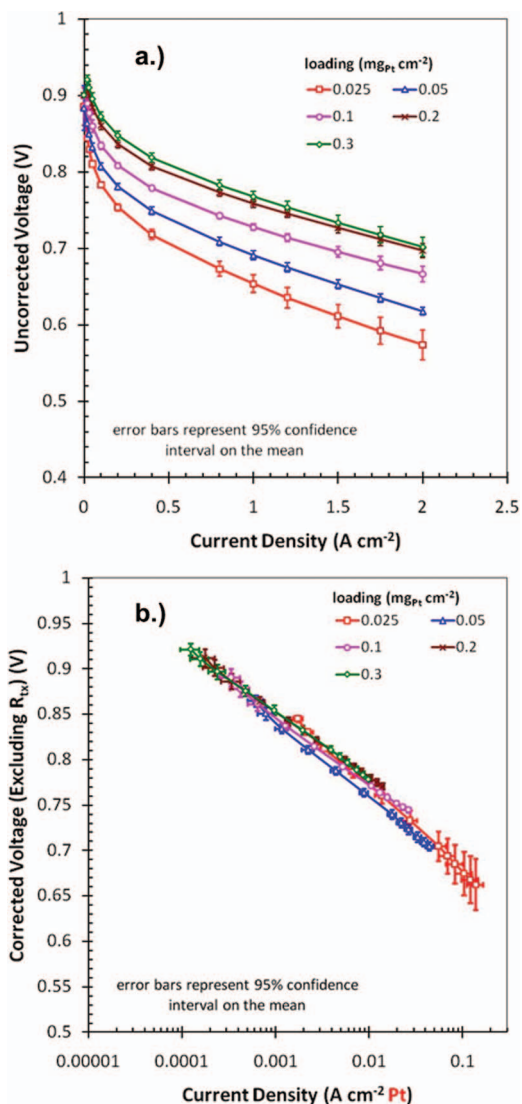
Figure 4. Non-diluted electrode performance with 100% H_2/O_2, 100% RH, 80C, 150 kPa operating conditions. a.) uncorrected performance; b.) HFR, electrode proton resistance, and hydrogen cross over corrected potential with current density scale to Pt area.

Figure 5. Non-diluted electrode performance with H_2/air, 100% RH, 80°C, 150 kPa operating conditions. a.) uncorrected performance; b.) HFR, electrode proton resistance, bulk transport, and hydrogen cross over corrected potential with current density scaled to Pt area.

Here, F is the Faraday constant and $C_{O_2,channel}$ is the oxygen concentration in the cathode channel at differential conditions. To gather multiple data points at low limiting current, oxygen concentrations of 0.01, 0.02, and 0.04 are considered at total pressures of 110, 150, 200, and 300 kPa (to evaluate the pressure dependent terms). Liquid water effects were minimized with differential flow controlled at 65% relative humidity.

Before further considering these limiting current results, Pt surface area was examined with polarization performance of the non-diluted electrode formulations (i.e. no additional bare carbon support). The pure oxygen performance in Figure 4a is corrected for HFR, electrode protonic resistance, and hydrogen crossover current in Figure 4b. Normalizing current density by Pt area on a logarithmic scale shows a relatively linear behavior, thus indicating most of the performance loss associated with reduced loading in Figure 4a is kinetic. However, for the same operating condition with air instead of oxygen (the analysis now including bulk transport corrections as oxygen concentration can vary significantly in air), performance shown in Figure 5 indicates an increasing transport loss as loading is decreased. In Figure 5b, the only transport loss not accounted for is the pressure independent term given in Figure 3g, which clearly varies as loading decreases. With this
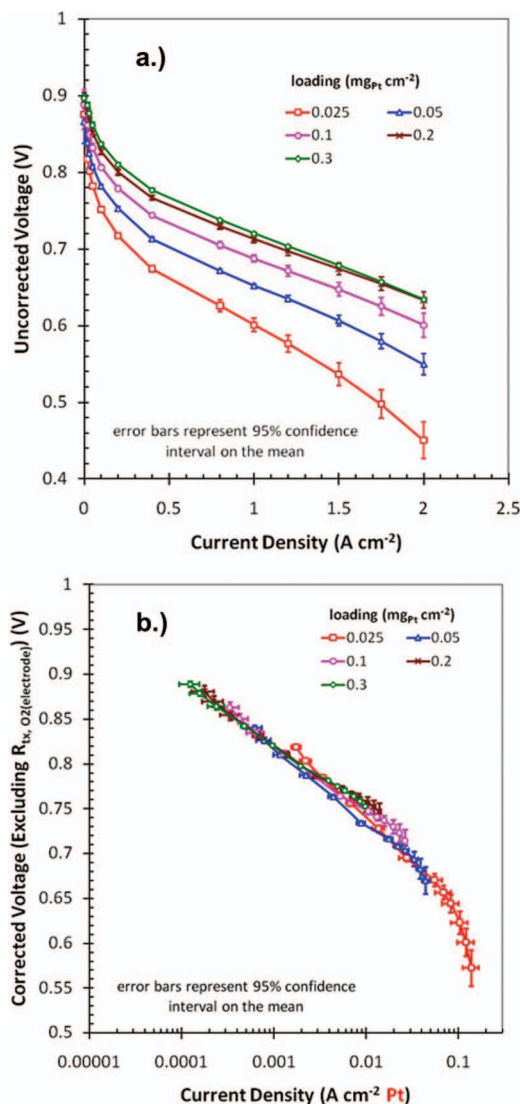
local transport loss now shown to increase with decreased Pt loading, a simple geometric correction is sought as a first approximation.

As assumed in Equation 1, a logical starting point is to scale based on the inverse of normalized Pt area. Since all bulk transport resistance has been shown to be relatively constant, the total transport resistance calculated from Equation 3 for each oxygen concentration at a given total pressure is considered as a function of loading according to Equations 1 and 2 in Figure 6. In Figure 6, the slope for a given total pressure represents the transport resistance near the Pt surface. This linear approximation fits the data fairly well, resulting in an average resistance of 4.8 s cm^{-1} at the Pt surface.

Next, to further consider if this resistance scales exclusively with Pt area, the performance of the carbon diluted electrodes is compared to the non-diluted samples. In oxygen this comparison shown in Figure 7a indicates nearly identical performance, with kinetic loss dominating. However, in air, for a given loading, a significant deviation between diluted and non-diluted samples is observed in Figure 7b-7c. Figure 7b provides a direct comparison to Figure 5, where all diluted electrodes at a given Pt loading show increased mass transport loss. A drier operating condition at 65% RH is given in Figure 7c, and the deviation between high and low wt% of Pt/C
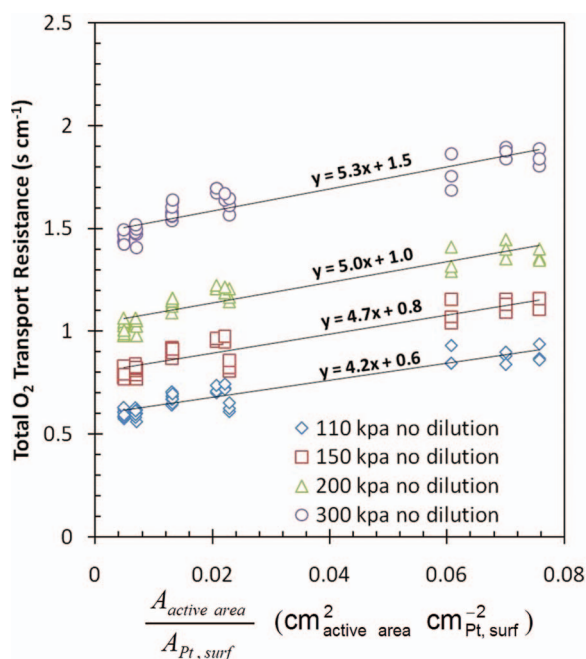
Figure 6. Total transport resistance calculated from Equation 4 for each oxygen concentration at a given total pressure as a function of Pt area for non-diluted catalyst layers.

Figure 7. Diluted compared with non-diluted performance; a.) H_2/O_2, 100% RH, 80°C, 150 kPa operating conditions b.) H_2/air, 100% RH, 80°C, 150 kPa operating conditions (non-diliuted data from Figure 5), c.) H_2/air, 65% RH, 80°C, 150 kPa operating conditions.

catalyst layers is observed to increase at these drier test points. This trend indicates that liquid water does not have a significant role in the observed performance loss between catalyst types at a given loading. Increased deviation at dry conditions was also confirmed with the 93.5°C polarization curve (not shown) described in Table I.

Additional characterization of the deviation between different catalyst dispersions in Figure 7 was executed at the lowest loading studied, where the performance deviation between catalyst types is most pronounced. The Pt dispersions at 0.025 mg_{Pt} cm^{-2} were further varied with different wt% Pt/Vulcan and bare Vulcan content as described in Table III (samples 7-12). These formulations expand on the 0.025 mg_{Pt} cm^{-2} performance given in Figure 7c by further demonstrating a direct correlation between performance loss and Pt dispersion with multiple data sets as shown in Figure 8 for the same operating condition. Here, performance loss seems to scale proportionally with increasing wt% Pt/Vulcan catalyst when current is normalized by geometric area in Figure 8a. In Figure 8b, current density is corrected for the measured gas crossover and scaled to Pt area with potential corrected for coverage dependent kinetics,[11] ohmic resistance, and changes in oxygen partial pressure in the electrode due to bulk and Knudsen transport resistances. Although the high wt% dispersions seem to scale with Pt area in Figure 8b, the more dispersed 5 and 7.5 wt% Pt/C samples clearly do not. This indicates that scaling directly to Pt surface area is not sufficient for all dispersed catalyst structures tested. Rather, at low loading, the dispersion (or equivalently the distance between Pt particles) should be considered.

To elucidate further, one can solve the oxygen diffusion equation for total oxygen transport resistance from the gas phase to the Pt surface, considering interfacial resistance at Pt/ionomer ($R_{Pt/i}$) and gas/ionomer interfaces ($R_{g/i}$), respectively, in addition to the bulk resistance of the ionomer film (R_f), as detailed in the appendix. In the platinized aggregates shown in Figure 1, multiple platinum nanoparticles sit on a carbon support particle coated with electrolyte. For oxygen transport through the thin ionomer film to the Pt surface where it is electrochemically reduced to water, we assume that the Pt particles are uniformly distributed on the surface of a carbon particle and thus only consider the case that a single Pt particle rests on a discrete carbon surface whereas the thin ionomer film of uniform thickness covers both Pt and carbon surfaces.
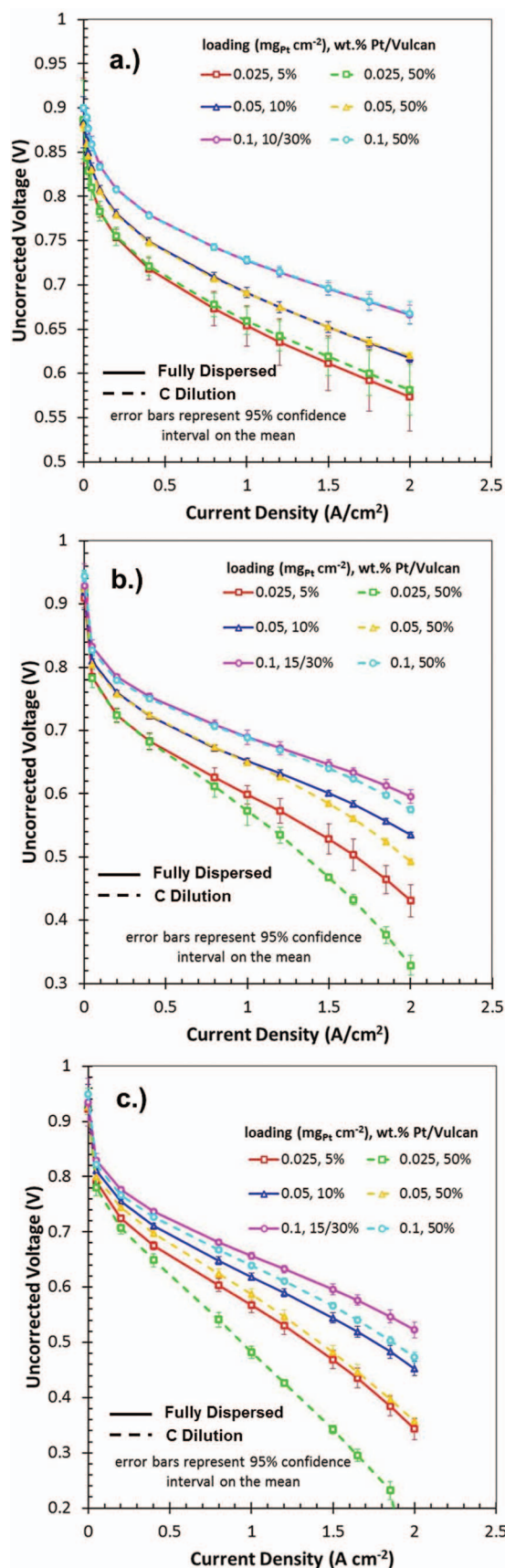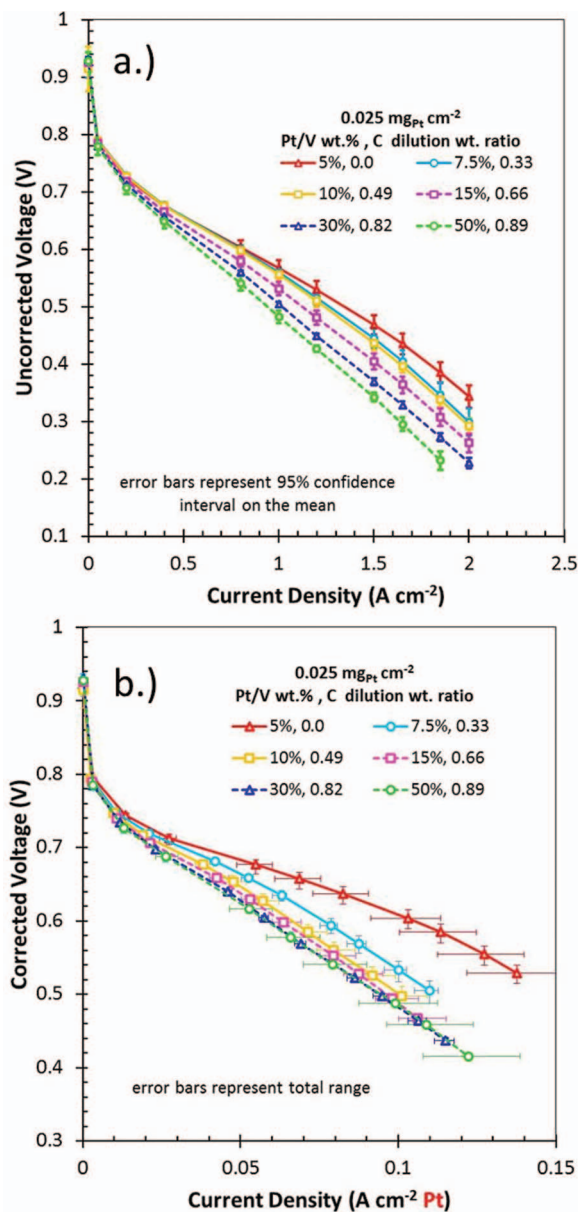
Figure 8. Loadings of 0.025 mg$_{Pt}$ cm^{-2} with varied bare carbon dilution (samples 7-12 in Table III) at H$_2$/air, 65% RH, 80°C, 150 kPa operating conditions, a.) uncorrected performance, b.) current density corrected for measured gas crossover and scaled to Pt area with potential corrected for coverage dependent kinetics, ohmic resistance, and changes in oxygen partial pressure in the electrode due to bulk and Knudsen transport resistance.

Using this single particle analysis based on an assumed constant particle size for all catalysts used in the current study, Figure 9 displays a parametrical study for various scenarios of bulk and interfacial resistances in the ionomer film. For comparison, the bulk and interfacial resistances were varied to match the measured local resistance value for the 5 wt% Pt/Vulcan (most dispersed) electrode first to compare the relative trends, and then the functionality of four film resistance scenarios was evaluated as the ratio of ionomer to Pt area approaches unity. It is shown that a resistance scenario focused on only one of the two interfaces will not agree with the measured local resistance that increases with the Pt particle density. If the interfacial resistances are ignored entirely, the film resistance must be an order of magnitude larger than bulk ionomer. Although the functionality of an increased bulk resistance scenario follows the trend observed experimentally in Figure 3g, the magnitude of increase from high to low dispersions of Pt
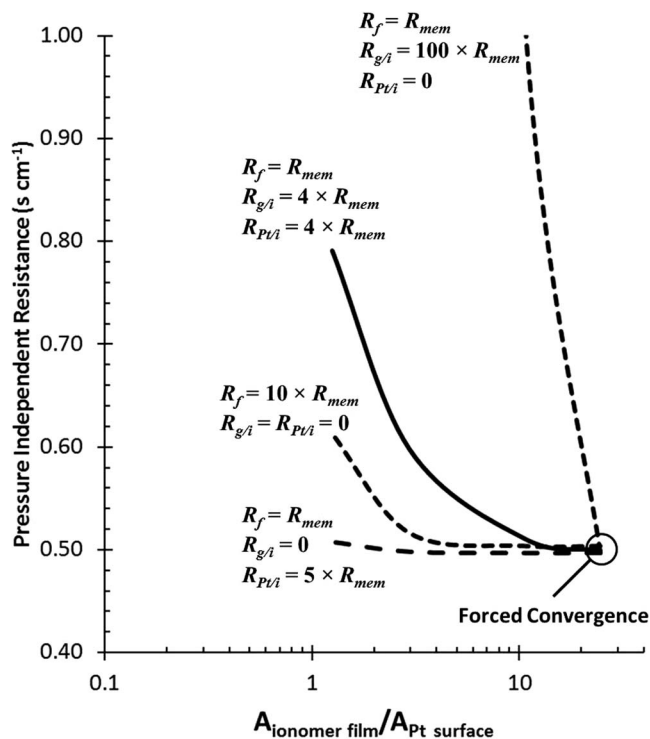

Figure 9. Model predictions showing the significance of interfacial resistances at both gas/ionomer and platinum/ioonomer interfaces. The model assumes 40 nm (in diameter) carbon particle, 60 m^2/g$_{Pt}$ HAD area, and 4 nm thick ionomer film.

will be under predicted. A final scenario that includes both interfacial resistances at a factor of 4 relative to bulk ionomer resistance (ca. 1 s cm^{-1}) and a film resistance equal to bulk ionomer shows a trend that most closely matches the data. This final scenario also makes the most sense physically, as it has been established that the resistance scales relatively well with Pt surface area (Figure 6) for higher dispersions at a given loading and it should be expected that a transport model would include a Pt interfacial resistance. Furthermore, the oxygen permeability through the bulk of the film remains at a realistic value with this scenario that includes two interfacial resistances.

A direct comparison of this model to the experimental results requires an average Pt particle size for each catalyst type. This is calculated from the measured electrochemical surface area given in Figure 2a and verified with XRD. In Figure 10a, the measured pressure independent transport resistance is compared to the model at different loadings with samples that have the highest dispersions of Pt (no bare carbon dilution). In the two model predictions shown, the Pt interfacial resistance is constant at 4 multiples of bulk and the gas side interfacial resistance is varied between 0 and 4 multiples of bulk. This comparison demonstrates that the model accurately captures the trend in the data as Pt loading is decreased without an interfacial resistance at the gas interface. This is due to the high area ratio of ionomer to Pt in these non-diluted samples at lower loadings. At high loading the Pt surface area is large enough to make the local transport effect negligible because of lower current per Pt area. The importance of the gas side interfacial resistance is only realized as the Pt particles get closer together and the oxygen flux through the ionomer/gas surface is near that at the Pt. This relationship is shown in Figure 10b at 0.025 mg$_{Pt}$ cm^{-2} where both resistances are required to predict the increase in transport resistance as the Pt becomes more concentrated.

This analysis shows that interfacial resistances might dominate the oxygen transport through a thin ionomer film (e.g. 4 nm) to the Pt surface. It is therefore desirable in the current state-of-the-art to reduce oxygen flux per unit area of ionomer coverage. Beyond the simplified analysis presented here, the observed differences in oxygen
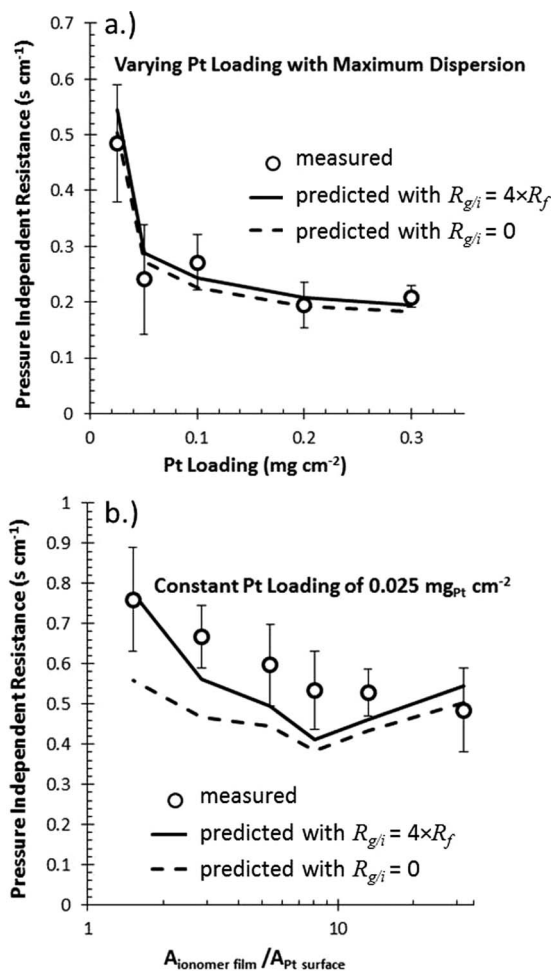
Figure 10. Pressure independent oxygen transport resistance from single particle model and experiments, a.) varying Pt loading with most dispersed samples (no bare carbon dilution), b.) constant Pt loading of 0.025 mg$_{Pt}$ cm^{-2} with varying Pt dispersions.

transport could also be accounted for with a more complex analysis of the mesoscale structure inside agglomerated platinized aggregates where the average transport length to the Pt surface varies. However, given the microscopy characterization results from this work and key parameters that were kept constant between samples, an agglomerate approach is difficult to justify. Regardless of the complexity of the geometry assumed, these applied experiments along with an oxygen limiting current analysis demonstrate that local oxygen transport loss can be partially mitigated with electrode design, where oxygen flux through the gas/ionomer interface to the Pt surface is minimized for a given electrode structure and catalyst type.

Conclusions

An experimental campaign was developed to study local oxygen transport resistance near the Pt surface in dispersed fuel cell electrodes. Platinum nano particle distributions were varied by diluting various wt% Pt on Vulcan catalysts with bare Vulcan to maintain a constant catalyst layer thickness, ionomer content, and macroscopic structure. The impact of Pt dispersion could then be studied by performance and limiting current methods without confounding issues related to the gas phase in the bulk of the catalyst layer. Results show that significant performance loss is realized with increased Pt particle density at a given Pt loading and the total transport resistance trends accordingly. With all other transport properties kept constant, the current experiments enable this trend in transport resistance to be

attributed not only to the actual Pt surface area but also the surface area of ionomer that covers the Pt and the carbon that surrounds it.

The physical origin of this transport resistance through a thin film of ionomer was further investigated by modeling limiting current at a single Pt particle. In this idealized case, the ratio of ionomer surface area relative to the Pt particle is used to consider the different wt% Pt/Vulcan catalysts. Within this domain the relative influence of theoretical transport restrictions at the gas and Pt surface was considered. Comparing the model to the experimental data revealed that both interfacial transport resistances must be prominent to account for the observed trend as wt% of Pt/Vulcan increases. Fundamentally, these experiments and analysis demonstrate that transport resistance through the ionomer coating is a function of both Pt surface area and Pt particle dispersion. Practically, this work has shown that local oxygen transport loss can be mitigated with electrode design, where oxygen flux through the gas/ionomer interface to the Pt surface must be minimized.

Appendix

In a platinized agglomerate shown in Figure 1, multiple platinum nano-particles sit on a carbon support particle coated with electrolyte. For oxygen transport through the thin ionomer film to the Pt surface where it is electrochemically reduced to water, one can assume that the Pt particles are uniformly distributed on the surface of a carbon particle and thus only consider the case that a single Pt particle rests on a private carbon surface whereas the thin ionomer film of uniform thickness covers both Pt and carbon surfaces. Approximately, it can be represented in the cylindrical coordinates as displayed in Figure A1.
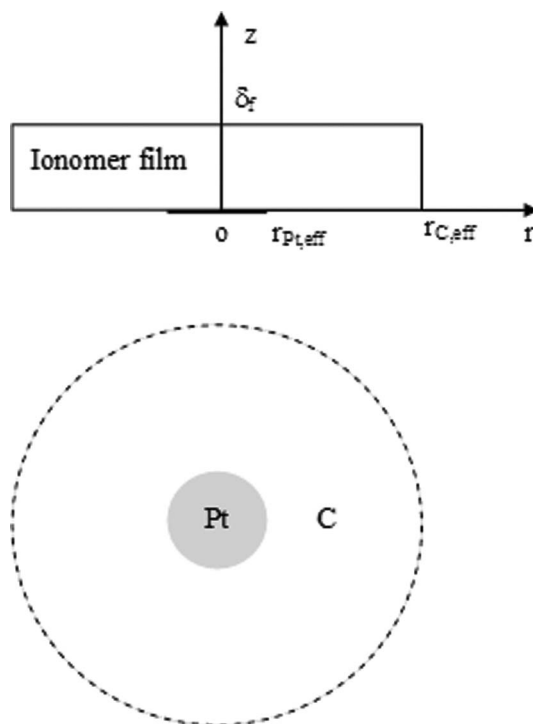

Figure A1. Schematic of the model representation of a single Pt particle on carbon support surface covered by a thin ionomer film.

Given the weight percentage of Pt, Pt particle size, and carbon support particle size, one can calculate the number of Pt particles on the surface of the carbon particle,

$$N_{Pt} = \frac{\rho_C}{\rho_{Pt}} \cdot \left(\frac{r_C}{r_{Pt}}\right)^3 \cdot \left(\frac{wt\%Pt}{100 - wt\%Pt}\right) \qquad [A1]$$

Where ρ is the density, r the radius, with subscripts C and Pt denote carbon and Pt particles, respectively. The effective radii shown in Figure A1 results from the surface area of the Pt particle,

$$r_{Pt,eff} = 2r_{Pt} \qquad [A2]$$

And from the surface area of the carbon particle and the number of Pt particles,

$$r_{C,eff} = \frac{2r_C}{\sqrt{N_{Pt}}} \qquad [A3]$$

The Pt particle size can be estimated based on the measured HAD area. Assuming spherical particle,

$$r_{Pt} = \frac{3}{\rho_{Pt} \cdot HAD} \qquad [A4]$$

Conservation of oxygen in the ionomer film gives

$$\frac{1}{r}\frac{\partial}{\partial r}\left(K_{O2}r\frac{\partial p_{O2}}{\partial r}\right) + \frac{\partial}{\partial z}\left(K_{O2}\frac{\partial p_{O2}}{\partial z}\right) = 0 \qquad [A5]$$

Where K_{O2} is the oxygen permeability in the ionomer film. Equation A5 can be reduced to 1-D by integrating it over ionomer film thickness δ_f,

$$\frac{\partial}{\partial r}\left(K_{O2}r\frac{\partial p_{O2}}{\partial r}\right) + \left[\left(K_{O2}\frac{\partial p_{O2}}{\partial z}\right)_{z=\delta_f} - \left(K_{O2}\frac{\partial p_{O2}}{\partial z}\right)_{z=0}\right]\frac{r}{\delta_f} = 0 \qquad [A6]$$

When measuring limiting current, oxygen partial pressure at the Pt surface approaches zero. Thus, one has

$$\left(K_{O2}\frac{\partial p_{O2}}{\partial z}\right)_{z=\delta_f} = \frac{p_{O2}^g - p_{O2}}{R_{g/i} + \frac{\delta_f}{2K_{O2}}} \qquad [A7]$$

and

$$\left(K_{O2}\frac{\partial p_{O2}}{\partial z}\right)_{z=0} = \begin{cases} 0, & \text{if } r > r_{Pt,eff} \\ \frac{p_{O2}}{R_{Pt/i} + \frac{\delta_f}{2K_{O2}}} & \text{if } r \le r_{Pt,eff} \end{cases} \qquad [A8]$$

Notice that in equations A7 and A8, interfacial resistance at both gas/ionomer and Pt/ionomer interfaces are considered. Utilizing equations A7 and A8 as well as the symmetric boundary condition at r = 0 and $r = r_{Pt,eff}$, Eq. A6 can be integtated over a control volume of Δr and then solved numerically to obtain oxygen pressure within each control volume of the ionomer film

$$p_{O2,i} = \frac{\frac{2r_{i-1}}{\Delta r_i + \Delta r_{i-1}}p_{O2,i-1} + \frac{2r_i}{\Delta r_i + \Delta r_{i+1}}p_{O2,i+1} + \frac{p_{O2}^g}{(2\beta_g+1)} \cdot \frac{r_i^2 - r_{i-1}^2}{\delta_f^2}}{\frac{2r_{i-1}}{\Delta r_i + \Delta r_{i-1}} + \frac{2r_i}{\Delta r_i + \Delta r_{i+1}} + \left(\frac{1}{2\beta_g+1} + \frac{\alpha}{2\beta_{Pt}+1}\right)\frac{r_i^2 - r_{i-1}^2}{\delta_f^2}} \qquad [A9]$$

For internal control volumes, and

$$p_{O2,i} = \frac{\frac{2r_i}{\Delta r_i + \Delta r_{i+1}}p_{O2,i+1} + \frac{p_{O2}^g}{(2\beta_g+1)} \cdot \frac{r_i^2}{\delta_f^2}}{\frac{2r_i}{\Delta r_i + \Delta r_{i+1}} + \left(\frac{1}{2\beta_g+1} + \frac{1}{2\beta_{Pt}+1}\right)\frac{r_i^2 - r_{i-1}^2}{\delta_f^2}} \qquad [A10]$$

for left-bound control volume (adjacent to r = 0), and

$$p_{O2,i} = \frac{\frac{2r_{i-1}}{\Delta r_i + \Delta r_{i-1}}p_{O2,i-1} + \frac{p_{O2}^g}{(2\beta_g+1)} \cdot \frac{r_i^2 - r_{i-1}^2}{\delta_f^2}}{\frac{2r_{i-1}}{\Delta r_i + \Delta r_{i-1}} + \left(\frac{1}{2\beta_g+1}\right)\frac{r_i^2 - r_{i-1}^2}{\delta_f^2}} \qquad [A11]$$

for the right-bound control volume (adjacent to $r = r_{C,eff}$). In Eq. A9, α takes 1 for the control volumes above Pt surface and 0 for those touching carbon surface. In Eq. A9 through A11, β is the ratio of interfacial resistance over the bulk resistance of the ionomer film, which is

$$\beta_k = \frac{R_{k/i}}{\left(\frac{\delta_f}{K_{O2}}\right)} \qquad k = g, Pt \qquad [A12]$$

Eq. A9 through A11 are iteratively solved for oxygen pressure distribution in the thin ionomer film. Then the limiting current density in the unit of A/cm^2_{Pt} can be calculated by the total oxygen flux to the Pt surface

$$i_{lim} = \frac{4F}{r_{Pt,eff}^2}\sum\frac{p_{O2,i}(r_i^2 - r_{i-1}^2)}{\left(R_{Pt/i} + \frac{\delta_f}{2K_{O2}}\right)} \qquad [A13]$$

And the local oxygen transport resistance in the unit of s/cm can be evaluated by

$$R_{O2}^{local} = \frac{4Fp_{O2}^g}{i_{lim}(RT \cdot 10^3)} \qquad [A14]$$

In the case that only one control volume is considered over the Pt surface, the local resistance becomes

$$R_{O2}^{local} = \left[\left(\beta_{Pt} + \frac{1}{2}\right) + \left(\beta_g + \frac{1}{2}\right)\left(\frac{r_{Pt,eff}}{r_{C,eff}}\right)^2\right]\frac{\delta_f}{K_{O2}(RT \cdot 10^3)} \qquad [A15]$$

which shows that the local resistance increases with the relative Pt surface area over carbon surface area. As a result, an electrode made of higher weight percentage of Pt/C would yield higher local transport resistance, as its relative Pt surface area is larger. The relative importance of an interfacial resistance can be extracted from the measured electrode resistance by the limiting current method.

List of Symbols

A	area, cm^2
C_{O2}	oxygen concentration, mol/cm^3
D	diffusion coefficient, cm^2/s
F	Faraday constant, 96487 C/eqiv.
HAD	Pt surface area measured by HAD, m^2/g
I_{lim}	limiting current density based on cell active area, A/cm^2
i_{lim}	limiting current density based on Pt surface area, Acm^2_{Pt}
K_{O2}	oxygen permeability, mol/(cm s kPa)
L_{Pt}	Pt loading, mg_{Pt}/cm^2
N_{Pt}	number of Pt particles on a single carbon particle
p_{O2}	oxygen partial pressure, kPa
R	universal gas constant, 8.314 J/(mol K)
r	r-axis in r-z coordinate, or radius, cm
r_i	r value of the center of i-th control volume, cm
R_f	bulk resistance of ionomer film, cm^2 s kPa/mol
$R_{k/i}$	interfacial resistance at phase k/ionomer interface, cm^2 s kPa/mol
R_{O2}	oxygen transport resistance, cm/s
T	temperature, K
Z	z-axis in r-z coordinate

Greeks

α	switch that take a value of 0 or 1 in Eq. A9
β	ratio of interfacial resistance over the bulk resistance as defined by Eq. A12
δ_f	thickness of ionomer film coating Pt/C catalyst, cm
ρ	density, g/cm^3

Sub/Superscripts

C	carbon
eff	effective
g	gas phase
g/i	gas phase/ionomer interface
lim	limiting
P,dep	pressure dependent
P,ind	pressure independent
Pt	platinum
Pt/i	platinum/ionomer interface
surf	surface

References

1. Y. Ono, T. Mashio, S. Takaichi, A. Ohma, H. Kanesaka, and K. Shinohara, *ECS Trans.*, **28**, 69 (2010).
2. K. Sakai, K. Sato, T. Mashio, A. Ohma, K. Yamaguchi, and K. Shinohara, *ECS Trans.*, **25**, 1193 (2009).
3. A. Ohma, T. Mashio, K. Sato, H. Iden, Y. Ono, K. Sakai et al., *Electrochim. Acta*, **56**, 10832 (2011).
4. X. Leimin, L. Shijun, Y. Lijun, and L. Zhenxing, *Fuel Cells*, **9**, 101 (2009).
5. A. D. Taylor, E. Y. Kim, V. P. Humes, J. Kizuka, and L. T. Thompson, *J. Power Sources*, **171**, 101 (2007).

6. A. Bonakdarpour, K. Stevens, G. D. Vernstrom, R. Atanasoski, A. K. Schmoeckel, M. K. Debe, and J. R. Dahn, *Electrochim. Acta*, **53**, 688 (2007).
7. P. Strasser, S. Koh, T. Anniyev, J. Greeley, K. More, C. Yu et al., *Nature Chem.*, **2**, 454 (2010).
8. V. R. Stamenkovic, B. Fowler, B. S. Mun, G. Wang, P. N. Ross, C. A. Lucas, and N. M. Markovic, *Science*, **315**, 493 (2007).
9. Y. Wang and C.-Y. Wang, *Electrochim. Acta*, **50**, 1307 (2005).
10. A. Kongkanand and P. K. Sinha, *J. Electrochem. Soc.*, **158**, B703 (2011).
11. N. P. Subramanian, T. A. Greszler, J. Zhang, W. Gu, and R. Makharia, *J. Electrochem. Soc.*, **159**, B531 (2012).
12. T. Mashio, A. Ohma, S. Yamamoto, and K. Shinohara, *ECS Trans.*, **11**, 529 (2007).
13. K. Kudo, T. Suzuki, and Y. Morimoto, *ECS Trans.*, **33**, 1495 (2010).
14. H. Iden, A. Ohma, K. Yamaguchi, and K. Shinohara, *ECS Trans.*, **25**, 907 (2009).
15. D. R. Baker, D. A. Caulk, K. C. Neyerlin, and M. W. Murphy, *J. Electrochem. Soc.*, **156**, B991 (2009).
16. S. K. Dishari and M. A. Hickner, *ACS Macro Lett.*, **1**, 291 (2012).
17. G. Beaucage, R. Composto, and R. S. Stein, *Journal of Polymer Science Part B: Polymer Physics*, **31**, 319 (1993).
18. J. A. Forrest and K. Dalnoki-Veress, *Adv. Colloid Interface Sci.*, **94**, 167 (2001).
19. B. Frank, A. P. Gast, T. P. Russel, H. R. Brown, and C. Hawker, *Macromolecules*, **29**, 6531 (1996).
20. J. L. Keddie, R. A. L. Jones, and R. A. Cory, *Faraday Discuss.*, **98**, 219 (1994).
21. A. Kongkanand, *J. Phys. Chem. C*, **115**, 11318 (2011).
22. J. A. Dura, V. S. Murthi, M. Hartman, S. K. Satija, and C. F. Majkrzak, *Macromolecules*, **42**, 4769 (2009).
23. H. Iden, K. Sato, A. Ohma, and K. Shinohara, *J. Electrochem. Soc.*, **158**, B987 (2011).
24. Z. Siroma, R. Kakitsubo, N. Fujiwara, T. Ioroi, S. I. Yamazaki, and K. Yasuda, *J. Power Sources*, **189**, 994 (2009).

25. J. Peron, D. Edwards, M. Haldane, X. Y. Luo, Y. M. Zhang, S. Holdcroft, and Z. Q. Shi, *J. Power Sources*, **196**, 179 (2011).
26. D. K. Paul, A. Fraser, and K. Karan, *Electrochem. Comm.*, **13**, 774 (2011).
27. R. Madhusudana Rao and R. Rengaswamy, *J. Power Sources*, **158**, 110 (2006).
28. D. Harvey, J. G. Pharoah, and K. Karan, *J. Power Sources*, **179**, 209 (2008).
29. J. Liu and M. Eikerling, *Electrochim. Acta*, **53**, 4435 (2008).
30. S. Obut and E. Alper, *J. Power Sources*, **196**, 1920 (2011).
31. M. Secanell, K. Karan, A. Suleman, and N. Djilali, *Electrochim. Acta*, **52**, 6318 (2007).
32. N. P. Siegel, M. W. Ellis, D. J. Nelson, and M. R. Von Spakovsky, *J. Power Sources*, **115**, 81 (2003).
33. W. Sun, B. A. Peppley, and K. Karan, *Electrochim. Acta*, **50**, 3359 (2005).
34. W. Yoon and A. Z. Weber, *J. Electrochem. Soc.*, **158**, B1007 (2011).
35. R. N. Carter, S. S. Kocha, F. Wagner, M. Fay, and H. A. Gasteiger, *ECS Trans.*, **11**, 403 (2007).
36. H. A. Gasteiger, S. S. Kocha, B. Sompalli, and F. T. Wagner, *Applied Catalysis B: Environmental*, **56**, 9 (2005).
37. Y. Liu, M. W. Murphy, D. R. Baker, W. Gu, C. Ji, J. Jorne, and H. A. Gasteiger, *ECS Trans.*, **11**(1), 473 (2007).
38. J. Zhang, B. Litteer, F. Coms, and R. Makharia, *ECS Trans.*, **41**, 1471 (2011).
39. K. C. Neyerlin, W. Gu, J. Jorne, A. Clark, Jr., and H. A. Gasteiger, *J. Electrochem. Soc.*, **154**, B279 (2007).
40. W. Gu, D. R. Baker, Y. Liu, and H. A. Gasteiger, Proton exchange membrane fuel cell (PEMFC)down-the-channel performance model, Chapter 43. *Handbook of Fuel Cells – Fundamentals, Technology and Applications*. Edited by Wolf Vielstich, Harumi Yokokawa, and Hubert A. Gasteiger. Volume 6: *Advances in Electocatalysis, Materials, Diagnostics and Durability*. 2009 John Wiley & Sons, Ltd.
41. Thomas A. Greszler, David A. Caulk, and Puneet K. Sinha, *J. Electrochem. Soc.*, **159**, F831 (2012).